$BaMgF_4$: An Ultra-Transparent Two-Dimensional Nonlinear Photonic Crystal with Strong $\chi^{(3)}$ Response in the UV Spectral Region

Luis Mateos, Mariola O. Ramírez, Irene Carrasco, Pablo Molina, Juan F. Galisteo-López, Encarnación G. Víllora, Carmen de las Heras, Kiyoshi Shimamura, Cefe Lopez, and Luisa E. Bausá*

Ferroelectric patterning is often used in advanced photonics and optoelectronic devices to increase their operational bandwidth and functionality, providing novel and unique performances. However, the extension of the ferroelectric structures to two-dimensional geometries is currently limited to very few oxides and phosphates systems, which constrains its current and future applications. Here, careful processing based on e-beam lithography and poling is employed to fabricate the first example of a two-dimensional nonlinear photonic crystal in Barium Magnesium Fluoride, $BaMgF_4$, a ferroelectric fluoride crystal with an extraordinary transparency ranging from the deep ultraviolet (≈126 nm) to the mid infrared (≈13 μm). The optical characterization shows the possibility of obtaining simultaneously up to three different Cerenkov-type second harmonic generation processes distributed in a conical geometry via $\chi^{(2)}$-quasi-phase-matching technique. Additionally, the remarkably high $\chi^{(3)}$ nonlinear response of $BaMgF_4$ crystal in the UV spectral region is exploited to demonstrate what is believed to be the highest direct UV-third harmonic generation conversion efficiency in a solid state system via pure $\chi^{(3)}$ nonlinear process. Together, the results highlight the outstanding opportunities offered by nonlinear photonic structures as innovative avenues to manipulate the light generation and control with reliable multifunctional optical character.

1. Introduction

Since the work on two-dimensional nonlinear photonic crystals (2DNLPC) proposed by Berger fifteen years ago,[1] a large variety of inverse ferroelectric domain patterns with a two-dimensional geometry have been designed and implemented to generate frequency conversion processes at multiple wavelengths and spatial directions.[2–7] Compared to the well known one-dimensional nonlinear ferroelectric structures, 2D modulation of $\chi^{(2)}$-nonlinear susceptibility allows the simultaneous access to several reciprocal lattice vectors at different angles, each of which stands for quasi-phase-matching processes (QPM) in a different wavelength/direction. The first experimental demonstration of non-collinear multi-directional QPM-SHG processes was reported by Broderick et al. in 2000,[2] leading to an intense research line in materials science and nonlinear optics, including the demonstration of novel nonlinear optical phenomena, namely, Cerenkov and Raman Nath nonlinear diffraction, nonlinear Talbot effect or self-accelerated beams,[4,8,9] as well as other relevant examples such as nonlinear Airy beams, simultaneous generation of second to fifth harmonic conical beams or compact-engineered path-entangled quantum light monolithic sources.[3,10,11] However, despite the outstanding opportunities offered by domain-patterned nonlinear photonic structures as innovative avenues for light generation and control, the amount of systems in which artificially engineered ferroelectric patterning has been accomplished is small, being reduced to no more than ten of the thousand plus ferroelectric crystals available. In particular, the fabrication of 2DNPC has been limited to the isomorphs $LiNbO_3$, $LiTaO_3$, and $RbTiOPO_4$ (RTP), $KTiOPO_4$ (KTP) crystals. This material constrain hampers the potential of next-generation multiport-operation-QPM devices, particularly in the deep UV and mid-IR wavelength regions, where the above mentioned nonlinear materials cannot be used. Note that, the employed nonlinear material is essential for the fabrication of VUV all solid state lasers or MIR-IR sources, both widely demanded in a large number of scientific and industrial applications including photochemical processes, semiconductor and integrated circuit processes, spectroscopy or medical applications.[12–16] In this work, we study the $BaMgF_4$ system (hereafter

---

L. Mateos, Dr. M. O. Ramírez, I. Carrasco,
Dr. P. Molina, Prof. C. de las Heras, Prof. L. E. Bausá
Dpto. Física de Materiales and Instituto Nicolás Cabrera
Universidad Autónoma de Madrid
Madrid, 28049, Spain
E-mail: mariola.ramirez@uam.es
Dr. J. F. Galisteo-López, Prof. C. Lopez
Instituto de Ciencia de Materiales de Madrid (CSIC)
Calle Sor Juana Inés de la Cruz 3, Madrid, 28049, Spain
Dr. E. G. Víllora, Prof. K. Shimamura
National Institute for Materials Center
1–1 Namiki, Tsukuba, 305–0044, Japan

DOI: 10.1002/adfm.201302588

BMF), a ferroelectric fluoride crystal with an extraordinary transparency ranging from the deep ultraviolet (≈126 nm) to the mid infrared (≈13 μm).[17,18]

The paper is structure at follows. On one side the fabrication of two-dimensional periodical arrays of inverted ferroelectric domains in BMF is demonstrated by direct electron beam writing (DEBW). The variety of reciprocal lattice vectors provided by the nonlinear $\chi^{(2)}$ modulation and the ferroelectric domain walls, along with the optical biaxial nature of BMF result in the simultaneous generation of three different Cerenkov-type SHG processes. These processes are all distributed in a conical geometry and involve different polarization states. This capability of the system to simultaneously phase-match several nonlinear interactions points out the feasibility of the broadband nature of the nonlinear response in these 2D photonic crystal, which is of additional interest considering the remarkable large transparency range of BMF. Note that owing to the intriguing enhancement of $\chi^{(2)}$ parametric processes by domain walls,[19,20] Cerenkov-type SHG processes are not restricted to a particular lattice period and so the generated conical nonlinear response can be tuned over a large spectral range.[20,21] In particular the transparency range in the UV region may permit the access to the shortest wavelengths ever reported via nonlinear frequency-mixing process by crystalline materials.

On the other side, BMF presents relatively large third-order nonlinear refractive indexes in the UV region, at least an order or magnitude larger than those of β-BaB_2O_4 (BBO), LiB_3O_5 (LBO), or $LiNbO_3$, which enables the observation of nonlinear phenomena associated with third order nonlinearities such as third harmonic generation (THG), self-phase modulation, super-continuum spectra or stimulated Raman scattering in the UV.[22,23] This feature has been exploited by the authors in the last section to demonstrate what we believe is the highest UV-THG conversion efficiency in a single solid state system via pure $\chi^{(3)}$ nonlinear process. Up to 5% conversion efficiency at around 380 nm is demonstrated by type II birefringent phase matching. The study of THG processes based on third-order electric susceptibility in BMF is of great interest not only due to the possibility to extend the frequency conversion processes to the UV spectral region, but also due to its potential applications in quantum optics since it may allow the direct generation of photon triplets via the reverse process of THG.[24–26] Only few works on pure efficient $\chi^{(3)}$ frequency conversion processes have been reported to date,[27,28] so that, the obtained results increase the multifunctional character and interest of BMF as optical material and open the possibility for the development of novel states of light from frequency converter solid state systems taking advantage of its huge transparency range.

2. Results and Discussion

BMF is an orthorhombic ferroelectric fluoride crystal with space group C_{2v}^{12} ($Cmc2_1$) belonging to the $BaMF_4$ family of pyroelectric fluorides (M = Mg, Mn, Fe, Co, Ni, Zn). Its ferroelectric transition temperature is at 990 °C. It shows a spontaneous polarization value of 6.6 $\mu C\ cm^{-2}$ with coercive fields in the range 4 to 24 kV cm^{-1}, depending on the applied frequency.[29] Ferroelectricity in this system arises from the displacement of Ba atoms along the polar axis, *c*, which is accompanied by the rotation of the MgF_6 octahedra around the Mg atoms.[29] Ferroelectric switching in BMF results in antiparallel 180° domains and has been demonstrated by two different techniques: conventional electric field poling by planar electrodes, and piezoelectric force microscopy in ultra-thin crystals (≈70 μm).[30,31] Periodically poled structures with a grating period $\Lambda = 6.6$ μm have been obtained by using photo-lithographically patterned electrodes. After the poling process, the transparency and nonlinear properties of the material remain unaltered and the demonstration of collinear UV second harmonic generation via quasi-phase matching process has been reported.[18] However, despite the superiority of BMF over other ferroelectric materials, namely, large transparency, low coercive field, high optical damage threshold or the possibility to incorporate optically active laser ions during its crystal growth,[32–35] ferroelectric domain reversal in BMF has been limited up to now to 1D patterning and therefore, to a single nonlinear process. In this work, ferroelectric domain engineering has been expanded to 2D geometry to fabricate 2DNLPC with reliable multifunctional optical character in a broad spectral range.

2.1. Ferroelectric Patterning. Fabrication of 2DNLPC Structure

Ferroelectric domain inversion in BMF was carried out via direct electron beam writing (DEBW) by means of a scanning electron microscopy driven by a nanolithography software. This technique was chosen because, opposite to other conventional techniques, it allows processing thick single ferroelectric crystals with great patterning versatility and without the need of any previous masking step. However, the physical mechanism underlying the switching process by DEBW differs from those of other more conventional switching techniques. Opposite to polarization reversal by planar switching electrodes, in the case of DEBW the electric field across the sample is highly inhomogeneous, as the one induced by a point source, exceeding the conventional switching fields by 2–3 orders of magnitude at the irradiated surface and decreasing down to practically zero (≈1 V cm^{-1}) beyond several hundred micrometers depth. Thus, the effect of the applied density charge plays a key role on the final size and shape of the inverted ferroelectric domains. **Figure 1**a–c shows as an example, the evolution of square lattices of inverted ferroelectric domains in BMF obtained upon different electronic charge densities ranging from 50 to 250 $\mu C\ cm^{-2}$. In all the cases, the diameter of the irradiated single motives was 20 μm with a separation distance between adjacent domains of 20 μm. No ferroelectric inversion is observed for charge densities below 50 $\mu C\ cm^{-2}$ (Figure 1a). On the other hand, increasing the applied density charge above the threshold value (Figure 1b) allows domain reversal to grow spontaneously, leading to uncontrolled domain merging, which may produce the reversal of the fully irradiated area (Figure 1c).

The domain growth mechanism using DEBW as a function of the applied charge can be analyzed in terms of the so called ferroelectric domain breakdown phenomenon.[36,37] In the frame of this model, the driving force for the domain formation is the condition of minimum free energy, that is, the decrease

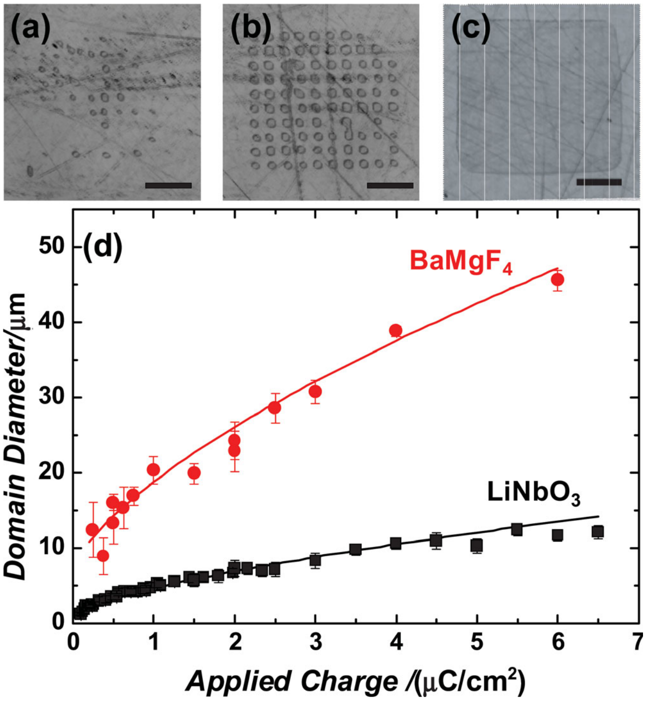

Figure 1. Optical micrographs of inverted ferroelectric domain patterns as a function of the electronic charge density in BaMgF$_4$. The scale bar is 100 µm. The diameter of the irradiated domains was 20 µm and the applied density charge was a) 50 µC cm^{-2}, b) 100 µC cm^{-2}, and c) 350 µC cm^{-2}. d) Lateral growth of the inverted ferroelectric domains as a function of the applied charge on BaMgF$_4$ (red dots) and LiNbO$_3$ (black squares). Solid lines correspond to the theoretical fit of the equilibrium domain size with the applied charge to a power law with exponent of 2/3.

of the total free energy of the system, which is composed of three main terms: the energy of the depolarization field, the surface energy of the domain walls, and the energy of the interaction between the domain and the applied electric field. Such a growth process results into string-like shaped domains, that is, inverted domains with a radius, *r*, considerably smaller than their length, *l*, ($r << l$), which exhibit a power law dependence on the applied charge equal to 2/3.[37] For BMF, the lateral growth of the inverted domains as a function of the applied charge is depicted in Figure 1d for inverted regions in the 10–50 µm range (solid circles). The crystal thickness was as large as 1 mm so that, the lateral size of the inverted domains is about 2 orders of magnitude smaller than their length, in agreement with the expected equilibrium dimensions for the system. Further, the domain radius power law dependence on the applied charge was found to be equal to 2/3 as predicted from theoretical calculations. Black squares in Figure 1d represent the equilibrium domain radius dependence on the applied charge obtained for LiNbO$_3$. The domain sizes are considerable lower than those in BMF for similar experimental conditions. The difference arises from the different value of their spontaneous polarization: 6.6 µC cm^{-2} versus 75–80 µC cm^{-2} for BMF and LiNbO$_3$, respectively, which ultimately determine domain breakdown in ferroelectrics. Indeed, the obtained results are in excellent agreement with the domain radius theoretically predicted ($\approx 1/P_s^{2/3}$).[37] At this point, we would like to mention that inversion of ferroelectric domains with a diameter inferior than 5µm was successfully achieved by DEBW in BMF, however, they were found to be unstable on time, disappearing after a few days. This is not the case of larger domains (≈10 µm), whose stability was confirmed after several months. On this basis, in order to obtain stable string-like ferroelectric domain superlattices with periodicities below 5 µm in BMF, a certain reduction on the crystal thickness must be required. Hence, the results displayed in Figure 1d provide the precise applied charge values required for tailoring a determined structure of ferroelectric domains in BMF. **Figure 2** shows two optical images of 2D periodical patterns of ferroelectric domains with different sizes and filling factors irradiated on BMF according to the analysis above. The ferroelectric patterns were obtained in large areas (0.5 mm × 0.5 mm) as required for photonic applications. Spatially resolved micro-Raman spectroscopy was employed to confirm that the optical properties of the system remain unaltered after the irradiation process. This technique has shown to be a powerful tool to investigate possible perturbations in the local structure of crystalline material after polarization reversal.[38,39] The obtained spectra collected at the center of the original (non irradiated) and inverted regions are shown in Figure 2c. In both cases, a good agreement is obtained with the Raman spectrum previously reported for BMF crystals.[40] As observed, no differences can be detected either in the position of the Raman peaks or in the spectral widths, the obtained spectra being identical. That is, no structural changes are observed which means

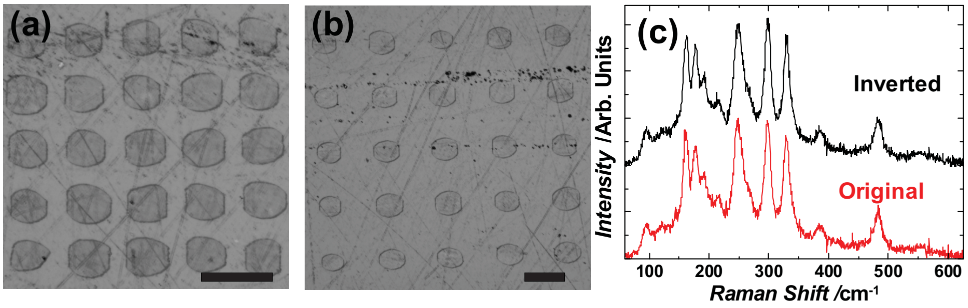

Figure 2. a,b) Optical images of two different 2D square lattices of inverted ferroelectric domains in BaMgF$_4$ crystal revealed after a selective chemical etching. The scale bar is 40 µm in both pictures. c) Room temperature Raman spectra collected at the original (non inverted) and domain inverted areas. The spectra have been vertically translated for the sake of comparison.

that electron bombardment is a suitable technique to produce domain inverted structures in BMF since the associated restructuring of the lattice and domain walls is taking place by preserving the optical characteristic of the crystal host.

2.2. Non Collinear Cerenkov-Type Second Harmonic Generation

As previously mentioned, an interesting feature of the 2D nonlinear photonic structure recorded in ferroelectric crystals is the possibility to generate nonlinear frequency conversion processes at multiple wavelengths/directions due to the vectorial character of the momentum conservation law. In this section we will focus on second harmonic generation (SHG). To analyze the multidirectional character of the fabricated $\chi^{(2)}$-NLPC a near infrared (λ = 1.06 µm) fundamental laser beam was launched along the polar direction. Upon this configuration, the whole set of reciprocal vectors lie in the plane perpendicular to the propagating beam. Thus, the momentum conservation law force a particular angular dispersion for the SHG beam defined by the trigonometrical relation: $\cos\alpha = 2k\omega/k_2\omega = n(\omega)/n(2\omega)$ where α refers to the conical angle between the propagating wave-vectors, $k\omega$ and $k_2\omega$, and $n(\omega)$ is the refractive index of the material at a frequency ω. In this case, two different nonlinear processes can be distinguished: the so-called nonlinear Bragg diffraction (NBD), where both the longitudinal and transverse phase matching conditions are simultaneously fulfilled, and the nonlinear Cerenkov radiation or Cerenkov-type SHG (CSHG), in which only the longitudinal phase matching condition is satisfied.[41] Though less efficient, the later (Cerenkov type parametric processes) has demonstrated to be a powerful tool to generate widely tunable multicolor radiation by means of a multistep $\chi^{(2)}$ cascade processes owing to the intriguing enhancement of $\chi^{(2)}$ parametric processes by domain walls.[19] Indeed, nonlinear Cerenkov radiation (in the form of two discrete symmetrically distributed SH spots) has been observed at a single localized domain wall.[20] The resulting nonlinear far field pattern obtained in both, NBD and CSHG exhibit the same conical angle α, since it is ultimately determined by the material refractive index dispersion. We will refer to it as Cerenkov angle.

At this point it is worthwhile to mention that due to the anisotropic nature of BMF, an electromagnetic wave propagating through the crystal parallel to the optical axis would split into two waves with perpendicular polarization, namely, the "slow" and "fast" waves. The two associated refractive indices n_s and n_f for the slow and fast waves, respectively, can be obtained by the two solutions of the Fresnel's equation and are listed in reference.[18] Because of its orthorhombic structure, BMF is optically biaxial, with the optical principal axes coincident with the crystallographic ones ($xyz \equiv bca$). This anisotropy has a strong impact on the generation of non-collinear CSHG: On the one hand, the refractive index values for the slow and fast waves will vary for every direction on the cone.[42] Hence, in 2D patterns the projection of the conical SH response on a screen would not be a circular ring but, in fact, it can show an elliptical shape. On the other hand, the permutation of the different slow/fast polarization states of the three involved waves can result in the simultaneous generation of several types of SHG processes. More specifically, in contrast to uniaxial materials where the maximum number of parametric processes is two (the so-called type I [*oo,o*] and type II [*oo,e*] SHG processes where two ordinary waves generate an ordinary/extraordinary SHG wave, respectively)[41] in biaxial systems up to six different SH processes can be simultaneously obtained, the final number being defined by the non-zero components of the second order nonlinear susceptibility tensor, $\chi^{(2)}$. In the particular case of BMF (mm2 symmetry), for a fundamental beam propagating parallel to the ferroelectric axis, *c*, the nonlinear polarization vector is given by: $P_c^{(2)} = d_{32}\cdot E_b^2 + d_{31}\cdot E_a^2$ where E_i denotes the electromagnetic field component of the fundamental beam along the $i = a,b$ crystallographic axis and d_{ij} are the involved second order nonlinear components. That is, SHG will be only generated in a non-collinear geometry exhibiting both slow and fast polarization components. On the other hand, the electric field polarization components of the fundamental beam are forced to be parallel to either *a* and *b* crystallographic axis, that is, slow and fast axes, respectively. Therefore, a maximum of four different (simultaneous) SH nonlinear interactions at the same frequency 2ω, but with different input/output polarization states can be obtained in a non-collinear configuration. The allowed non-collinear SH interactions can be written as: *ss-s*, *ss-f*, *ff-s*, and *ff-f*, where *s* and *f* refers to the slow and fast polarization, respectively. The two first letters denote the fundamental beam polarization, while the third one stands for the second harmonic generation.

For the experiments, two different ferroelectric domain patterns were considered: i) 1D periodically poled BMF (PPBMF) with a poling period $\Lambda \approx 17$ µm and ii) a 2D square lattice of inverted ferroelectric domains with $\Lambda \approx 20$ µm. **Figure 3**a–f shows the schematic of the experimental setup, the fabricated NLPCs and the generated far field SHG patterns, respectively. In all the cases, the polarization state of the fundamental beam was $\gamma = 0$, that is, parallel to the fast axis (*b* crystallographic direction). As seen, marked differences in the nonlinear response are obtained when the array of inverted domains is extended from 1D to 2D geometry. Indeed, the far field SHG pattern evolves from two symmetrical bright spots distributed at an angle of $\alpha^{\text{ext}} = 8.7$, to two concentrically conical patterns at external angles of $\alpha_1^{\text{ext}} = 8.7°$ and $\alpha_2^{\text{ext}} = 18°$ exhibiting azimuthal intensity modulation. The "transition" from discrete SHG pairs to a ring shaped geometry results from the 2D modulation of the $\chi^{(2)}$ second order nonlinear susceptibility and from the ferroelectric domain walls. In fact, the inner ring exhibit the same conical angle than that observed for the 1D ferroelectric structure. However, the number of nonlinear processes that can be simultaneously observed differs in each case. Note that the 1D ferroelectric structure only displays two peripheral bright spots distributed at the corresponding conical angle while the 2D pattern exhibit two concentric rings. More specifically, the outer ring observed in 2DNLPC is absent in the PPBMF (Figure 3c,f). This feature has nothing to do with the ferroelectric patterning but it is related to the non homogeneous azhimutal intensity profile of the generated beams and will be analyzed in detail in the next section.

The measured external angles were found to be in agreement with the Cerenkov relation $k_{2\omega}\cos\alpha = 2k_\omega$ for the *ff-f* ($\alpha = 8.12°$) and *ff-s* ($\alpha = 17.28°$) nonlinear processes, where the refractive

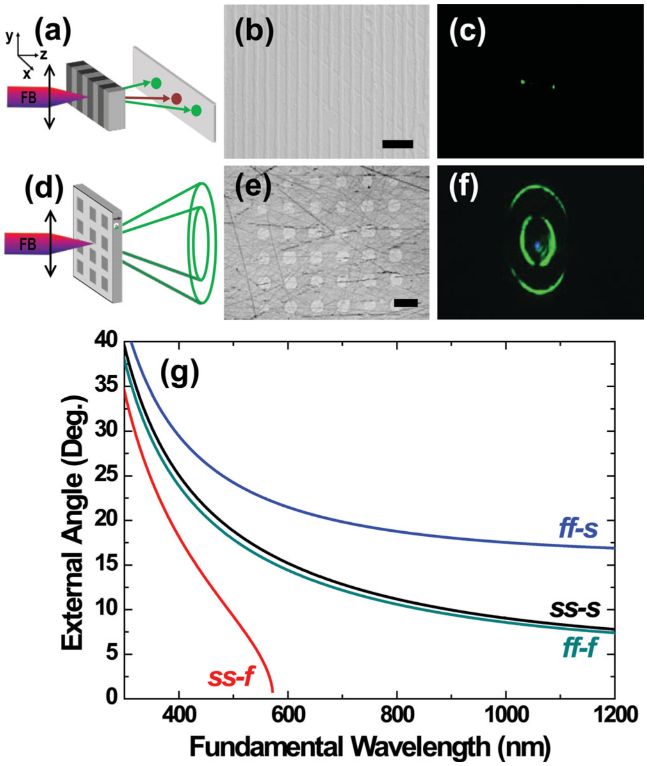

Figure 3. From left to right: Schematic of the experimental set-up used for Cerenkov type Second Harmonic generation process when the fundamental beam propagates parallel to the ferroelectric axis, optical picture of the employed ferroelectric structures and far field Cerenkov type SHG patterns obtained in a–c) 1D ferroelectric structures and d–f) 2D non linear photonic crystal. The scale bar is 40 μm. g) Calculated angular dependence of the generated SH beams as a function of the fundamental wavelength for the four allowed Cerenkov type SHG processes in $BaMgF_4$.

index values along *b* and *a* axis were employed as the values for the fast and slow waves, respectively. This approximation strongly simplified the mathematical treatment and was adopted on the basis of the small angular dispersion values and the nearly circular shape obtained for the nonlinear conical beams in BMF (Figure 3f)—note that the observable elliptical shape in the far field images is a consequence of the angular perspective from where the pictures were taken. The relationship between the external and internal angle was obtained by means of Snell's equation using the refractive index values given by Villora et al.[18] The calculated Cerenkov angular dispersion (external angle) for the four allowed CSHG processes as a function of the fundamental wavelength is shown in Figure 3g. As observed, the shorter the wavelength the larger the conical angle, being the maximum angular deflection obtained for the *ff-s* process. The minimum dispersion occurs for the *ss-f* which, in fact, cannot be observed for fundamental wavelengths larger than ≈570 nm. On the other hand, the *ss-s* and *ff-f* parametric processes will be generated at closely separated angles ($\Delta\alpha \approx 0.4°$), thus they will spatially overlap, unless the appropriate input/output polarization conditions are selected. We will go to this aspect next.

2.1.1. Azimuthal Intensity Modulation of the Cerenkov-SHG Beams. Polarization Properties

As pointed out, the generated conical beams feature a non homogenous azimuthal intensity distribution which results in noticeably different nonlinear far field SH patterns for the inner and outer rings, respectively (see Figure 3f). In particular, the far field pattern obtained for the inner ring displays two intensity maxima symmetrically distributed with respect to the vertical axis of the screen. On the contrary, the intensity maxima for the outer ring are symmetrical with respect to the horizontal axis. Indeed, the azimuthal angles at which the SH intensity reach its maximum values in the inner ring coincides with the minimum (zero) SH intensity registered for the outer ring and vice versa. Moreover, the azimuthal intensity profile can be modified by changing the polarization angle of the fundamental beam.

Figure 4a,b shows the far field SHG patterns obtained for fundamental beams linearly polarized along the slow and fast optical axis ($\gamma = \pi/2$ and $\gamma = 0$, respectively). As seen, when the input polarization of the incoming fundamental beam is rotated by $\pi/2$ the outer ring vanishes and the spatial intensity

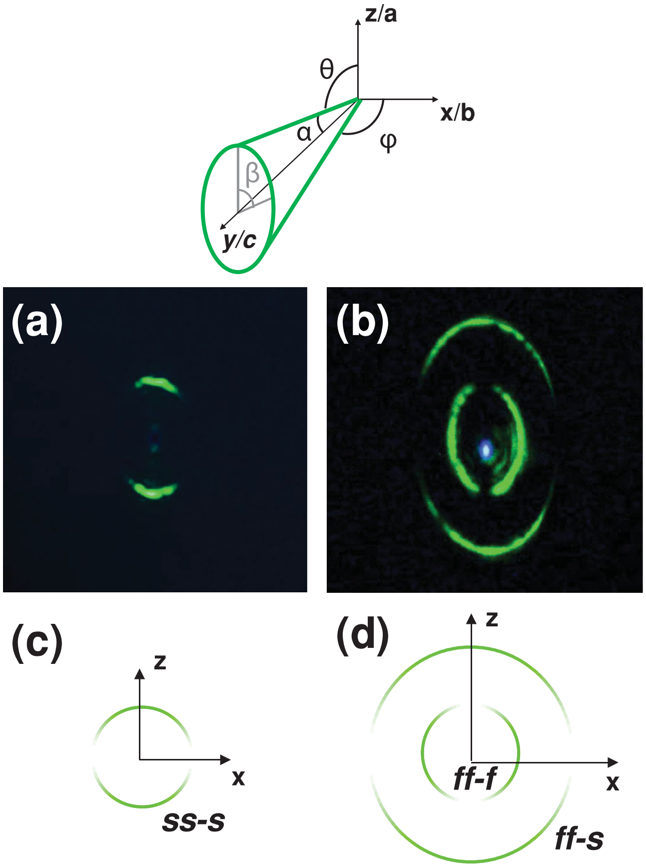

Figure 4. Far field Cerenkov type SHG patterns obtained in $BaMgF_4$ based 2DNLPC for linearly polarized fundamental beams with polarization states a) parallel to slow axis ($\gamma = \pi/2$) and b) parallel to fast axis ($\gamma = 0$); Calculated azimuthal dependence of the SH intensity for c) *ss-s*, and d) *ff-f* and *ff-s* processes from Equation 1. A schematic diagram of the involved angles is depicted on top of the figure.

distribution of the SHG pattern is modified. This can be explained by considering the different Cerenkov type SHG processes accessible in BMF.

The azimuthal intensity profile and polarization properties of the SHG patterns are defined by the $\chi^{(2)}_{ijk}$ nonlinear tensor associated with the space group of the nonlinear material and the effective nonlinearity involved in the parametric process, d_{eff}. In our case, according to the mm^2 point group symmetry of BMF, the effective nonlinearities responsible for the four allowed processes at any direction can be written as:

$$\begin{aligned} d_{\text{eff}}^{ss-s} &= (\cos\theta\sin\varphi\cos\delta + \cos\varphi\sin\delta)\, d_{31}\sin^2\gamma \\ d_{\text{eff}}^{ss-f} &= (-\cos\theta\sin\varphi\sin\delta + \cos\varphi\cos\delta)\, d_{31}\sin^2\gamma \\ d_{\text{eff}}^{ff-s} &= (\cos\theta\sin\varphi\cos\delta + \cos\varphi\sin\delta)\, d_{32}\cos^2\gamma \\ d_{\text{eff}}^{ff-f} &= (-\cos\theta\sin\varphi\sin\delta + \cos\varphi\cos\delta)\, d_{32}\cos^2\gamma \end{aligned} \tag{1}$$

where θ and φ refers to the spherical coordinates, γ is the input polarization angle, and the angle δ is defined by: $\cot\delta = \frac{\cot^2 V_Z \sin^2\theta + \sin^2\varphi - \cos^2\theta\cos^2\varphi}{\cos\theta\sin 2\varphi}$ being V_Z the angle between the optical axis and the z axis given by $V_z = \frac{n_z\left(n_y^2 - n_x^2\right)^{1/2}}{n_y\left(n_z^2 - n_x^2\right)^{1/2}}$.[43] In the particular case of nonlinear CSHG, the generated waves propagate at an angle α with respect to the c crystallographic direction (y axis). Therefore both, the θ and φ angles, can be written in terms of the propagating conical angle, α, as: $\theta = \frac{\pi}{2} - \alpha\cos\beta$, and $\varphi = \frac{\pi}{2} - \alpha\sin\beta$, where β refers to the azimuthal angle on the conical pattern. An schematic diagram in shown in Figure 4. The calculated intensity distribution of the *ss-s*, *ff-f* and *ff-s* parametric processes are shown in Figure 4c,d. As seen, the experimental results are in good agreement with the calculated profiles. Note that for the input linear polarization employed in Figure 3c ($\gamma = 0$) the *ff-s* parametric process vanished along the x axis. Thus, a single nonlinear process must be observed in 1D periodically poled BMF, according to the results displayed in Figure 3c. Here, we would like to recall that the employed fundamental beam ($\lambda_\omega = 1064$ nm) prevents the observation of the *ss-f* process, which, as mentioned above, is restricted to fundamental wavelengths shorter than ≈570 nm (Figure 3g).

Concerning the polarization state of the ring shaped Cerenkov radiation, it was found to be radial for the three types of parametric processes, according to the employed non-collinear experimental scheme and the symmetry of the SHG tensor in BMF. The polarization properties of the generated conical waves are imposed by the quadratic nonlinear susceptibility tensor, and therefore by the aforementioned expression for the nonlinear polarization vector ($P_c^{(2)} = d_{32}\cdot E_b^2 + d_{31}\cdot E_a^2$). Accordingly, the polarization state of the conical SHG is forced to be radial, regardless the polarization state of the incident beam. The effect of the different combinations of the input/output polarization states on the generated SHG patterns is shown in **Figure 5**. Three main features can be observed: first, it is possible to obtain each process in an independent manner; second, the *ss-f* process does not lead to any SHG signal (central panel) in agreement with the angular dispersion of the CSHG for fundamental wavelengths larger than ≈570 nm; third, up to three different CSHG processes can be simultaneously obtained when the slow and fast polarization states of the incident beam are selected at once. This is an exclusive property of biaxial crystals, which allows the generation of multiple harmonic conical waves spatially separated at their corresponding Cerenkov angles. In addition, we would like to highlight that in all the cases, the mm2 point group symmetry of the crystal is imprinted in the generated nonlinear far field SHG pattern, in agreement with previous work based on the directionality of the SHG response and the use of 2DNLPC for symmetry studies.[44,45]

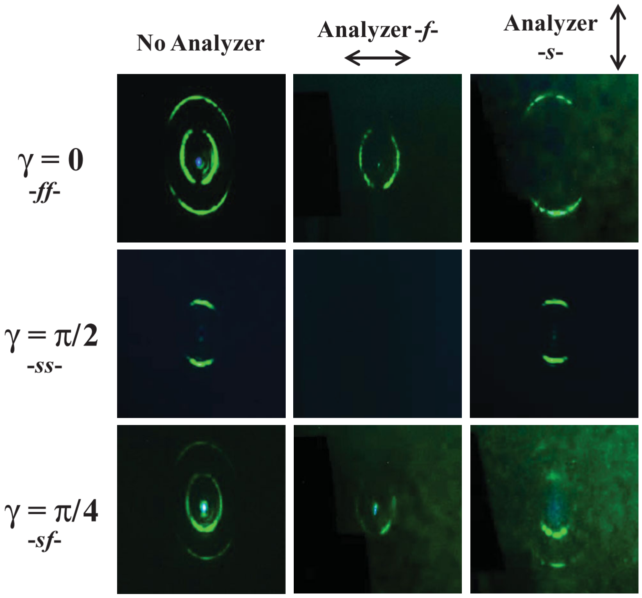

Figure 5. Far field Cerenkov type SHG patterns generated with different input-output polarization configurations. From top to bottom: Input linear polarization parallel to fast -*ff*- ($\gamma = 0$), slow -*ss*- ($\gamma = \pi/2$), and rotated $\pi/4$ from the fast axis -*sf*- ($\gamma = \pi/4$). The SHG output polarization was selected with an analyzer as follows: No analyzer (left column), fast -*f*- polarization (central column), slow polarization -*s*- (right column).

2.3. UV-Third Harmonic Generation Via $\chi^{(3)}$ Nonlinear Processes

In the previous section we have shown the possibility of obtaining simultaneously up to three types of CSHG processes distributed on a conical geometry via different $\chi^{(2)}$ nonlinear processes supported by the 2D ferroelectric patterning. Here, we demonstrate that additional frequency conversion processes, such as collinear THG, are also possible in the BMF crystal. In fact, phase-matched frequency tripling process can be achieved in the UV spectral region by means of birefringent phase matching (BPM) via the nonlinear susceptibility tensor, $\chi^{(3)}$. The study of THG processes based on third-order electric susceptibility in BMF is of great interest not only due to the possibility to extend the frequency conversion processes to the UV spectral region, but also due to its potential applications in quantum optics since it may allow the direct generation of photon triplets via the reverse process of THG.[24–26] Hence, each triplet would originate from a single pump photon and therefore quantum

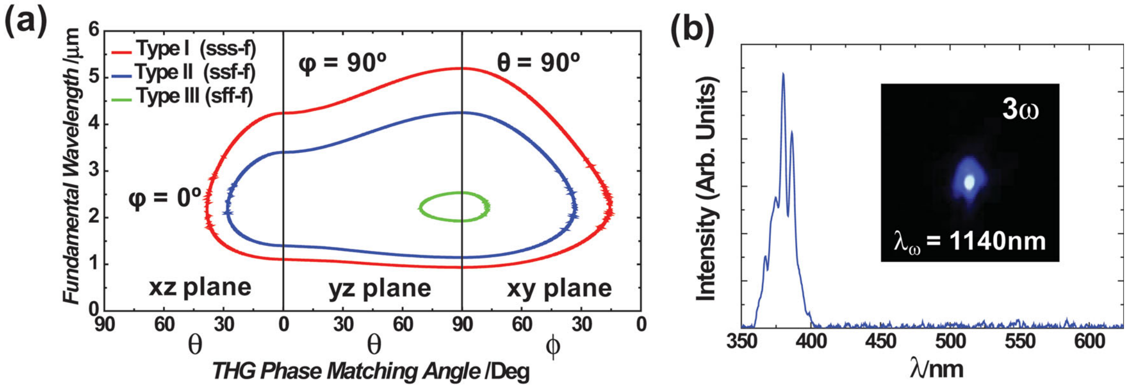

Figure 6. a) Birefringent phase matching curves for direct Type I, II, and III THG processes in the principal planes of $BaMgF_4$. b) Third harmonic generation spectrum obtained for a Type II BPM process when the fundamental beam ($\lambda_\omega = 1140$ nm) propagates parallel to the polar axis. The inset shows the far field image of the THG at 380 nm.

correlations will extend over all three photon. In addition to the striking quantum properties based on the three photons down conversion, efficient phase-matched THG at the UV region can be expected in BMF due to the recently reported large third-order nonlinearities in this system.[19,20]

The conditions for THG via $\chi^{(3)}$ frequency-mixing of three fundamental photons are calculated for birefringent-matching in BMF. Three different types of THG processes satisfy the energy and momentum conservation law, namely, Type I (*sss-f*), Type II (*ssf-f*), and Type III (*sff-f*) nonlinear interactions, where the three first letters refers to the polarization of the fundamental waves, and the last one represents the polarization of the THG beam. The calculated BPM curves for each type of THG in the principal planes ($\phi = 0°$, $\phi = 90°$, and $\theta = 90°$) is shown in **Figure 6**a. From this graph the conditions for non critical phase matching directions (and therefore, walk-off compensated) for a fundamental beam parallel to the ferroelectric axis were found to be 935 nm and 5200 nm for type I, 1146 nm and 4250 nm for type II, and 1930 nm and 2536 nm for type III processes. However, the non-zero components of the third-order nonlinear susceptibility tensor restrict the polarization conditions for the fundamental and THG beams. In particular, for BMF crystal (mm^2 symmetry) there are only 9 independent non-zero third order nonlinear coefficients, (χ_{11}, χ_{22}, χ_{16}, χ_{24}, χ_{18}, χ_{29}, χ_{33}, χ_{35}, χ_{37}).[46] Thus, the cubic polarization vector components of the THG wave for a fundamental beam travelling along the polar axis are given by:

$$\begin{aligned} P_a^{(3)} &= \chi_{11} \cdot E_a^3 + 3\chi_{18} \cdot E_a E_b^2 \\ P_b^{(3)} &= \chi_{22} \cdot E_b^3 + 3\chi_{29} \cdot E_a^2 E_b \\ P_c^{(3)} &= 0 \end{aligned} \tag{2}$$

a and *b* being the slow and fast directions, respectively ($n_a > n_b$). Hence, pure $\chi^{(3)}$ non critical THG by BPM can only be obtained via type II nonlinear interaction.

A tunable optical parametric amplifier generating 140 fs pulses at a repetition rate of 1 kHz was tuned at around 1140 nm to check the type II phase-matching condition for the direct cubic process in BMF. The linear polarization of the input beam was rotated $\pi/4$ from the *a* axis so that both slow and fast polarization components can be simultaneously used. Figure 6b shows the experimental results (THG spectrum, $\lambda_{THG} = 380$ nm) obtained with a 1 mm long *z*-cut BMF crystal at room temperature, when the fundamental beam travels along the polar axis. Let us recall that for a fundamental beam travelling parallel to the ferroelectric axis, collinear SHG is not allowed by symmetry restrictions. Consequently, THG via two steps $\chi^{(2)}$-cascade process will not contribute to the generated signal. This is in agreement with the manifested lack of SHG signal at 570 nm. Thus, direct cubic interaction is confirmed as responsible of the observed UV-THG in BMF. At this point, it is interesting to note the large spectral width obtained for the BPM nonlinear process, which exhibit a full width at half maximum value, FWHM ≈ 17 nm. This fact is mainly related to the spectral broadening of the femtosecond pulsed laser used as excitation source (FWHM ≈ 50 nm), which allows for certain wavelength tunability by taking advantage of the spectral tolerance of the nonlinear THG process. More specifically, the phase-matching spectral bandwidth for a birefringent THG can be obtained from:

$$I^{TH} \propto \left(\frac{L}{\lambda}\right)^2 \operatorname{sinc}^2\left(\frac{\Delta k\, L}{2}\right) \tag{3}$$

being I^{TH} the intensity of the third harmonic wave, L the crystal length, λ the fundamental wavelength, and Δk the mismatch between the fundamental and TH waves. Thus, for 1 mm thick crystal, the theoretical spectral bandwidth expected for Type II THG process at 1146 nm is $\Delta\lambda \approx 14$ nm in good agreement with our experimental results. Dashed line in **Figure 7**a shows the calculated spectral tolerance for the cubic nonlinear process. Solid circles in the same graph represent the normalized THG intensity obtained when the fundamental wavelength was tuned from 1080 to 1230 nm. As seen, a certain spectral tunability can be obtained around 1146 nm, due to the large spectral bandwidth of the employed fs-pulsed fundamental laser beam. Indeed, the obtained tuning range can be well fitted by means of the convolution between ≈50 nm width gaussian pulses and the calculated bandwidth of the THG process defined by Equation 3. The results of the calculation are plotted in solid line. The very good agreement between the experimental and calculated spectral acceptances indicates that the effective

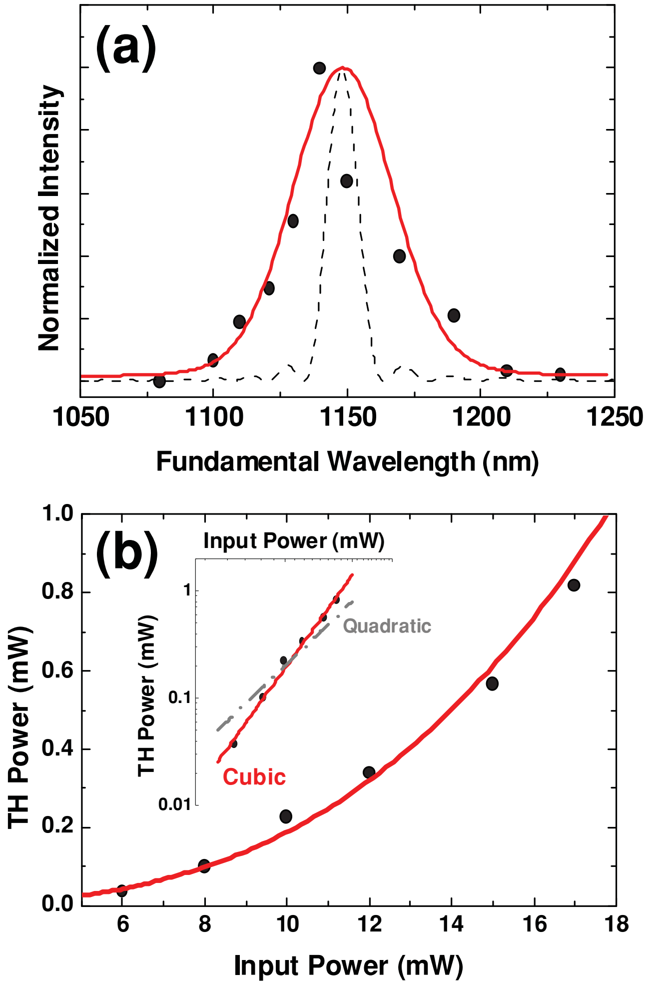

Figure 7. a) Experimental (solid dots) and calculated (dashed line) spectral tolerance for the $\chi^{(3)}$-direct Type II THG process in $BaMgF_4$. The solid line represents the convolution between Gaussian pulses with FWHM of 50 nm and the calculated bandwidth of the THG process. b) Average output power at 380 nm as a function of the incident power when the fundamental wavelength is tuned at 1140 nm. Dots and red line refer to experimental and theoretical cubic fit, respectively. The inset depicts the output power dependence in log scale along with the fittings (solid lines) to square and cubic dependence on the input power.

interaction length corresponds to the whole crystal length *L*. Figure 7b shows the pump power dependence between the fundamental beam at 1140 nm and the THG beam. The measured conversion shows a cubic power dependence with an efficiency that nearly reaches 5% for an input power of 17 mW (see inset in Figure 7b). This conversion efficiency is, to the best of our knowledge, the highest reported for pure cubic $\chi^{(3)}$-THG. Note that even though THG conversion efficiencies as large as 11% have been reported, they are accompanied by cascading quadratic processes.[47,48] Indeed, there are only few works in which efficient pure third order optical parametric interactions have been reported.[27,28] Higher input power results in the generation of a super-continuum spectrum. This phenomenon could be related with a self-phase modulation effect due to the short pulses and the nonlinearity of the medium, becoming one of the main limitation of the THG output power in BMF. Super-continuum generation is out of the scope of the current work and will be further studied in the future.

3. Conclusion

We have demonstrated the ability of ultra-transparent BMF ferroelectric crystal to operate as advanced multiport optical system from which second and third harmonic generation can be obtained in the UV-VIS spectral range. The simultaneous generation of multiple nonlinear processes in a single solid state system has been made feasible by combining highly efficient pure cubic $\chi^{(3)}$-third harmonic generation process in the UV spectral region and multiple quasi-phase matching second order nonlinear interactions in a fully dense square lattice of alternate ferroelectric domains. The nonlinear ferroelectric structure has been obtained after careful processing using e-beam writing, and constitutes the first example of a two-dimensional nonlinear photonic crystal in a fluoride system. Up to three different Cerenkov-type SHG processes distributed in a conical geometry via $\chi^{(2)}$ processes are demonstrated upon 1.06 μm infrared pumping, pointing out the feasibility of the nonlinear structure to continuously obtain widely tunable conical type quadratic SHG processes in this system. Let us recall that in contrast to nonlinear Bragg diffraction processes where the exact fulfillment of the full vectorial phase matching condition is required, the nonlinear Cerenkov radiation represents the type of nonlinear interaction in which only the longitudinal PM condition is fulfilled. As a result, the conical angle is defined by the material refractive index dispersion and the generated $\chi^{(2)}$ conical SHG response can be tuned in a broad spectral range by simply varying the fundamental wavelength. In this respect, the 2D patterned BMF crystal can be useful for the development of novel all optical solid state tunable devices operating from the mid-infrared (≈13 μm) up to VUV spectral region (≈125 nm) with the additional advantage of multi-directional response.

Additionally, the efficient pure cubic $\chi^{(3)}$-third harmonic generation process obtained in BMF allows to envisage novel sources of entanglement from which photon triplets via spontaneous parametric down conversion processes can be obtained with interesting applications in advanced quantum cryptography where a third photon can operate as control signal. Other functionalities such as continuous wave multidirectional self-frequency converter solid state laser or self-nonlinear prism can be also pictured in BMF due to the possibility of incorporating active laser ions in the crystal.

4. Experimental Section

Crystal Growth: BMF single crystals were grown by the Czochralski technique using a 30 kW R.F.-generator. High purity powders (99.99%) of commercially available BaF_2 and MgF_2 weighted and mixed in a Pt crucible. The crystal was grown under CF_4 (99.99%) gas.

Two-Dimensional Ferroelectric Patterning: A 1 mm thick plate from a single domain $BaMgF_4$ crystal was cut and polished with its main faces oriented perpendicular to the ferroelectric c-axis. The ferroelectric domain pattern was fabricated via direct electron beam writing by means of a Philips XL30 Schottky field emission gun electron microscope driven by an Elphy Raith nanolithography software. The electron beam was focused on the -c face of the crystal without any mask. Prior to the irradiation process, a 100 nm film of Al was deposited on the +c face, which acted as a ground electrode during the electron irradiation. The acceleration voltage was 15 kV and the current beam 0.3 nA. The applied density charge was varied between 50 and 350 μC cm^{-2}.The inverted domains were directed along the polar axis of the crystal (*c* axis) and crossed the whole thickness of the sample. The lateral size of the inverted domain columns ranged between 5 and 20 μm for which the lattice parameter of the squared array varied between 15 and 50 μm, respectively. The spatial extension of the patterns use in this work was 0.5 mm × 0.5 mm. The inverted ferroelectric domain structures were revealed after a selective chemical etching in a solution of HCl.

Confocal Spectroscopy: Micro-Raman experiment was performed at room temperature in a laser scanning confocal microscope. An Ar$^+$ laser at 488 nm was used as excitation sources. The laser beam was focused onto the sample by a microscope objective. The Raman response was collected in backscattering geometry with the same objective (50× magnification, numerical aperture, NA = 0.75 in air) and focused into a multi-mode fiber. The end of the fiber was directly connected to the spectrometer and the signal detected with a Peltier-cooled charge coupled device camera. A beam splitter and notch filter were used to attenuate the pump laser line. The sample was placed on a 2-axis XY motorized stage with 0.2 μm spatial resolution thus, precise positioning of the sample under the laser spot was achieved. The laser was focused to a spot diameter smaller than 1 μm.

Cerenkov-type SHG Experiments: A ps-laser at 1064 nm (Spectra Physics Navigator) with a repetition rate of 20 kHz was employed as incidental beam. All the frequency conversion experiments were performed with the fundamental beam travelling parallel to the ferroelectric axis. A polarizer and a half wave plate were used to control the input polarization state of the beam. The generated non-collinear second harmonic response was projected on a white screen and its polarization properties were analysed with a second polarizer. The far field pictures of the generated conical radiation were obtained by means of Nikon D90 digital camera.

Third Harmonic Generation via $\chi^{(3)}$ Sum-Frequency-Mixing: An ultrafast Optical Parametric Amplifier (Coherent OPerA-Solo) generating 140 fs pulses at a repetition rate of 1 kHz was used as tunable excitation source for the third harmonic generation experiments. The laser beam was focused to a spot size of about 100 μm and the polarization of the fundamental beam was controlled by a linear polarizer and a half-wave plate. The spectrum of the THG was collected by an Ocean Optics HR4000 spectrometer and the THG power output was measured by a Coherent FieldMax-TO power meter.

Acknowledgements

This work has been supported by FP7 NoE Nanophotonics4Energy EU grant No. 248855; the Spanish MICINN CSD2007–0046 (Nanolight.es), MAT2010–17443, MAT2012–31659 (SAMAP) and the Comunidad de Madrid S2009/MAT-1756 (PHAMA) projects.

Received: July 31, 2013
Revised: September 5, 2013
Published online: November 4, 2013

---

[1] V. Berger, *Phys. Rev. Lett.* **1998**, *81*, 4136.
[2] N. G. R. Broderick, G. W. Ross, H. L. Offerhaus, D. J. Richardson, D. C. Hanna, *Phys. Rev. Lett.* **2000**, *84*, 4345.
[3] T. Ellenbogen, N. Voloch-Bloch, A. Ganany-Padowicz, A. Arie, *Nat. Photonics* **2009**, *3*, 395.
[4] S. M. Saltiel, D. N. Neshev, R. Fischer, W. Krolikowski, A. Arie, Y. S. Kivshar, *Phys. Rev. Lett.* **2008**, *100*, 103902.
[5] H. Y. Leng, X. Q. Yu, Y. X. Gong, P. Xu, Z. D. Xie, H. Jin, C. Zhang, S. N. Zhu, *Nat. Commun.* **2011**, *2*, 429.
[6] K. Gallo, A. Pasquazi, S. Stivala, G. Assanto, *Phys. Rev. Lett.* **2008**, *100*, 053901.
[7] H. X. Li, S. Y. Mu, P. Xu, M. L. Zhong, C. D. Chen, X. P. Hu, W. N. Cui, S. N. Zhu, *Appl. Phys. Lett.* **2012**, *100*, 101101.
[8] Y. Zhang, J. Wen, S. N. Zhu, M. Xiao, *Phys. Rev. Lett.* **2010**, *104*, 183901.
[9] I. Dolev, I. Kaminer, A. Shapira, M. Segev, A. Arie, *Phys. Rev. Lett.* **2012**, *108*, 113903.
[10] L. Mateos, P. Molina, J. Galisteo, C. Lopez, L. E. Bausa, M. O. Ramirez, *Opt. Express* **2012**, *20*, 29940.
[11] H. Jin, P. Xu, X. W. Luo, H. Y. Leng, Y. X. Gong, W. J. Yu, M. L. Zhong, G. Zhao, S. N. Zhu, *Phys. Rev. Lett.* **2013**, *111*, 023603.
[12] F. K. Tittel, D. Richter, A. Fried, in *Solid-State Mid-Infrared Laser Sources*, Vol. *89* (Eds: I. T. Sorokina, K. L. Vodopyanov), Springer, Berlin, Germany **2003**, pp 445–510.
[13] D. Cyranoski, *Nature* **2009**, *457*, 953.
[14] R. D. Schaeffer, T. Hannon, *Laser Focus World* **2001**, *37*, 115.
[15] R. Steiner, in *Mid-Infrared Coherent Sources and Applications*, (Eds: M. Ebrahim-Zadeh, I. Sorokina), Springer, Netherlands **2008**, p 575.
[16] L. J. Kugler, M. X. Wang, *Appl. Opt.* **2010**, *49*, F1.
[17] K. Shimamura, E. G. Villora, K. Muramatsu, N. Ichinose, *J. Cryst. Growth* **2005**, *275*, 128.
[18] E. G. Villora, K. Shimamura, K. Sumiya, H. Ishibashi, *Opt. Express* **2009**, *17*, 12362.
[19] N. An, H. Ren, Y. Zheng, X. Deng, X. Chen, *Appl. Phys. Lett.* **2012**, *100*, 221103.
[20] X. Deng, X. Chen, *Opt. Express* **2010**, *18*, 15597.
[21] M. O. Ramirez, P. Molina, L.E. Bausá, *Opt. Mat.* **2012**, *34*, 524.
[22] J. Chen, X. Chen, A. Wu, H. Li, Y. Zheng, Y. Ma, L. Jiang, J. Xu, *Appl. Phys. Lett.* **2011**, *98*, 191102.
[23] Y. Ma, J. Chen, Y. Zheng, X. Chen, *Appl. Opt.* **2012**, *51*, 5432.
[24] J. Douady, B. Boulanger, *Opt. Lett.* **2004**, *29*, 2794.
[25] H. Hubel, D. R. Hamel, A. Fedrizzi, S. Ramelow, K. J. Resch, T. Jennewein, *Nature* **2010**, *466*, 601.
[26] K. Bencheikh, F. Gravier, J. Douady, A. Levenson, B. Boulanger, *C. R. Phys.* **2007**, *8*, 206.
[27] J. P. Feve, B. Boulanger, Y. Guillien, *Opt. Lett.* **2000**, *25*, 1373.
[28] F. Gravier, B. Boulanger, *Opt. Express* **2006**, *14*, 11715.
[29] K. Shimamura, E. G. Villora, H. Zeng, M. Nakamura, S. Takekawa, K. Kitamura, *Appl. Phys. Lett.* **2006**, *89*, 232911.
[30] S. C. Buchter, T. Y. Fan, V. Liberman, J. J. Zayhowski, M. Rothschild, E. J. Mason, A. Cassanho, H. P. Jenssen, J. H. Burnett, *Opt. Lett.* **2001**, *26*, 1693.
[31] H. Zeng, K. Shimamura, E. G. Villora, S. Takekawa, K. Kitamura, *Phys. Scripta* **2007**, *T129*, 108.
[32] J. G. Bergman, G. R. Crane, H. Guggenheim, *J. Appl. Phys.* **1975**, *46*, 4645.
[33] E. G. Villora, P. Molina, S. Alvarez, J. V. Garcia-Santizo, M. O. Ramirez, K. Shimamura, L. E. Bausa, *J. Appl. Phys.* **2010**, *107*, 033106.
[34] J. E. Muñoz-Santiuste, H. Loro, R. Marino, Ph. Goldner, V. Vasyliev, E. G. Villora, K. Shimamura, P. Molina, M. O Ramírez, L. E. Bausá, *Phys. Rev. B* **2012**, *85*, 184110.
[35] J. V. Garcia-Santizo, B. del Rosal, M. O. Ramirez, L. E. Bausa, E. G. Villora, P. Molina, V. Vasyliev, K. Shimamura, *J. Appl. Phys.* **2011**, *110*, 063102.
[36] L. Mateos, L. E. Bausa, M. O. Ramirez, *Appl. Phys. Lett.* **2013**, *102*, 042910.
[37] M. Molotskii, A. Agronin, P. Urenski, M. Shvebelman, G. Rosenman, Y. Rosenwaks, *Phys. Rev. Lett.* **2003**, *90*, 107601.

[38] R. Hammoum, M. D. Fontana, P. Bourson, V. Y. Shur, *Appl. Phys. A Mater.* **2008**, *91*, 65.
[39] G. Stone, D. Lee, H. Xu, S. R. Phillpot, V. Dierolf, *Appl. Phys. Lett.* **2013**, *102*, 042905.
[40] F. Kubel, H. Hagemann, H. Bill, *Z. Anorg. Allg. Chem.* **1997**, *623*, 573.
[41] S. M. Saltiel, Y. Sheng, N. Voloch-Bloch, D. N. Neshev, W. Krolikowski, A. Arie, K. Koynov, Y. S. Kivshar, *IEEE J. Quantum Elect.* **2009**, *45*, 1465.
[42] X. Yin, S. Zhang, Z. Tian, *Opt. Laser Technol.* **2007**, *39*, 510.
[43] V. G. Dmitriev, D. N. Nikogosyan, *Opt. Commun.* **1993**, *95*, 173.
[44] L. Mateos, P. Molina, L. E. Bausa, M. O. Ramirez, *Appl. Phys. Express* **2011**, *4*, 082202.
[45] P. Molina, M. O. Ramirez, B. J. Garcia, L. E. Bausa, *Appl. Phys. Lett.* **2010**, *96*, 261111.
[46] C. C. Shang, H. Hsu, *IEEE J. Quantum Elect.* **1987**, *23*, 177.
[47] P. S. Banks, M. D. Feit, M. D. Perry, *J. Opt. Soc. Am. B* **2002**, *19*, 102.
[48] K. Miyata, V. Petrov, F. Noack, *Opt. Lett.* **2011**, *36*, 3627.